2015

First measurement of the cross-correlation of CMB lensing and galaxy lensing

Nicky Hand

Alexie Leauthaud

Sudeep Das

Blake D. Sherwin

Bruce Partridge
Haverford College, bpartrid@haverford.edu

First measurement of the cross-correlation of CMB lensing and galaxy lensing

Nick Hand,[1,*] Alexie Leauthaud,[2] Sudeep Das,[3,4] Blake D. Sherwin,[5,6,4] Graeme E. Addison,[7] J. Richard Bond,[8] Erminia Calabrese,[9] Aldée Charbonnier,[10,11] Mark J. Devlin,[12] Joanna Dunkley,[9] Thomas Erben,[13] Amir Hajian,[8] Mark Halpern,[7] Joachim Harnois-Déraps,[7,8,14] Catherine Heymans,[15] Hendrik Hildebrandt,[13] Adam D. Hincks,[7] Jean-Paul Kneib,[16,17] Arthur Kosowsky,[18] Martin Makler,[11] Lance Miller,[19] Kavilan Moodley,[20] Bruno Moraes,[11,21,22] Michael D. Niemack,[23] Lyman A. Page,[24] Bruce Partridge,[25] Neelima Sehgal,[26] Huanyuan Shan,[16] Jonathan L. Sievers,[20,24,8] David N. Spergel,[27] Suzanne T. Staggs,[24] Eric R. Switzer,[28,8] James E. Taylor,[29] Ludovic Van Waerbeke,[7] Charlotte Welker,[30,31] and Edward J. Wollack[28]

[1]*Department of Astronomy, University of California, Berkeley, California 94720, USA*
[2]*Kavli Institute for the Physics and Mathematics of the Universe (WPI), Todai Institutes for Advanced Study, University of Tokyo, Kashiwa, Chiba 277-8582, Japan*
[3]*High Energy Physics Division, Argonne National Laboratory, 9700 South Cass Avenue, Lemont, Illinois 60439, USA*
[4]*Berkeley Center for Cosmological Physics, Berkeley, California 94720, USA*
[5]*Department of Physics, University of California, Berkeley, California 94720, USA*
[6]*Miller Institute for Basic Research in Science, University of California, Berkeley, California 94720, USA*
[7]*Department of Physics and Astronomy, University of British Columbia, 6224 Agricultural Road, Vancouver, British Columbia V6T 1Z1, Canada*
[8]*Canadian Institute for Theoretical Astrophysics, University of Toronto, Toronto, Ontario M5S 3H8, Canada*
[9]*Sub-department of Astrophysics, University of Oxford, Keble Road, Oxford OX1 3RH, United Kingdom*
[10]*Observatório do Valongo, Universidade Federal do Rio de Janeiro, Ladeira do Pedro Antônio 43, Saúde, Rio de Janeiro RJ 20080-090, Brazil*
[11]*Centro Brasileiro de Pesquisas Físicas, Rua Doutor Xavier Sigaud 150, Rio de Janeiro RJ CEP 22290-180, Brazil*
[12]*Department of Physics and Astronomy, University of Pennsylvania, 209 South 33rd Street, Philadelphia, Pennsylvania 19104, USA*
[13]*Argelander Institute for Astronomy, University of Bonn, Auf dem Hügel 71, 53121 Bonn, Germany*
[14]*Department of Physics, University of Toronto, 60 St. George Street, Toronto, Ontario M5S 1A7, Canada*
[15]*Scottish Universities Physics Alliance, Institute for Astronomy, University of Edinburgh, Royal Observatory, Blackford Hill, Edinburgh EH9 3HJ, United Kingdom*
[16]*Laboratoire d'Astrophysique (LASTRO), Ecole Polytechnique Fédérale de Lausanne (EPFL), Observatoire de Sauverny, CH-1290 Versoix, Switzerland*
[17]*Aix Marseille Université, CNRS, LAM (Laboratoire d'Astrophysique de Marseille) UMR 7326, 13388 Marseille, France*
[18]*Department of Physics and Astronomy, University of Pittsburgh, Pittsburgh, Pennsylvania 15260, USA*
[19]*Department of Physics, University of Oxford, Keble Road, Oxford OX1 3RH, United Kingdom*
[20]*Astrophysics and Cosmology Research Unit, School of Mathematical Sciences, University of KwaZulu-Natal, Durban 4041, South Africa*
[21]*Department of Physics and Astronomy, University College London, Gower Street, London WC1E 6BT, United Kingdom*
[22]*CAPES Foundation, Ministry of Education of Brazil, Brasilia/DF 70040-020, Brazil*
[23]*Department of Physics, Cornell University, Ithaca, New York 14853, USA*
[24]*Department of Physics, Princeton University, Princeton, New Jersey 08544, USA*
[25]*Department of Physics and Astronomy, Haverford College, Haverford, Pennsylvania 19041, USA*
[26]*Department of Physics and Astronomy, Stony Brook University, Stony Brook, New York 11794-3800, USA*
[27]*Department of Astrophysical Sciences, Peyton Hall, Princeton University, Princeton, New Jersey 08544, USA*
[28]*NASA/Goddard Space Flight Center, Greenbelt, Maryland 20771, USA*

[29]*Department of Physics and Astronomy, University of Waterloo, Waterloo, Ontario N2L 3G1, Canada*
[30]*Institut d'Astrophysique de Paris, 98 bis boulevard Arago, 75014 Paris, France*
[31]*UPMC Paris VI, 4 place Jussieu, 75005 Paris, France*
(Received 24 November 2013; published 2 March 2015)

We measure the cross-correlation of cosmic microwave background (CMB) lensing convergence maps derived from Atacama Cosmology Telescope data with galaxy lensing convergence maps as measured by the Canada-France-Hawaii Telescope Stripe 82 Survey. The CMB-galaxy lensing cross power spectrum is measured for the first time with a significance of 4.2σ, which corresponds to a 12% constraint on the amplitude of density fluctuations at redshifts ~ 0.9. With upcoming improved lensing data, this novel type of measurement will become a powerful cosmological probe, providing a precise measurement of the mass distribution at intermediate redshifts and serving as a calibrator for systematic biases in weak lensing measurements.

DOI: 10.1103/PhysRevD.91.062001 PACS numbers: 98.62.Sb, 98.70.Vc

I. INTRODUCTION

The cosmic web of matter gravitationally deflects the paths of photons as they traverse the Universe—an effect known as gravitational lensing. In the case of light from the cosmic microwave background (CMB), these lensing deflections imprint information about the density fluctuations between the primordial universe at $z \sim 1100$ and the present day onto the observed CMB sky, and in doing so modify the statistical properties of the CMB anisotropies. Similarly, cosmological information about the lower-redshift universe can be extracted from the lensing-induced distortion of the shapes of galaxies, an effect referred to as weak lensing. In both cases, precise measurements of the small magnification and shear effects can be used to reconstruct the convergence field, which is a direct measure of the projected matter density [1,2].

Previous analyses have demonstrated the sensitivity of CMB lensing to the large-scale dark matter distribution through cross-correlations with sources that trace the same structure in the low-redshift universe. To date, several galaxy catalogs, the cosmic infrared background, and quasars have been shown to be well correlated with the CMB lensing convergence field [3–8]. Here, we report the first cross-correlation between CMB lensing and galaxy lensing through a measurement of the lensing-lensing cross power spectrum. The detection is a direct measure of the mass distribution localized to intermediate redshifts solely through the gravitational effects of lensing. It is also nearly insensitive to residual systematics that are independent in both data sets, providing a robust test of the Lambda cold dark matter (ΛCDM) model on the largest cosmic scales.

Lensing measurements are sensitive to both the expansion and growth histories of the Universe [9–11]. Separately, measurements of CMB lensing [12–15] and galaxy lensing [16–18] have already contributed to strong constraints on the amplitude of matter fluctuations and the nature of dark energy. Correlating weak lensing effects on the CMB and galaxies can break previous parameter degeneracies and offer powerful constraints on the evolution and nature of dark energy, the amplitude of matter fluctuations, and the sum of neutrino masses [19–21]. Furthermore, the cross-correlation will serve as an important calibrator of systematics and biases in optical and infrared cosmic shear experiments [22,23], which could otherwise limit future surveys [24].

Measurements of CMB lensing have matured quickly in recent years. Its effects were first detected in cross-correlation using radio-selected galaxy catalogs with WMAP data [25,26] and in autocorrelation using Atacama Cosmology Telescope (ACT) data [27]. Subsequent improvements to the lensing power spectrum were reported by the South Pole Telescope [14], ACT [12], and the Planck Collaboration [15]. Further advances in CMB lensing data are expected from multiple experiments in the near future [28–30]. Noting the anticipated enhancements of upcoming wide-field cosmic shear surveys [31,32], this work represents a first step in the application of a future, powerful tool for precision cosmology.

The measurement of the lensing-lensing cross power spectrum presented here uses CMB data from the Atacama Cosmology Telescope and optical lensing data from the Canada-France-Hawaii Telescope (CFHT) Stripe 82 Survey (CS82). The paper is structured as follows. Section II presents a brief overview of the theoretical expectation for the cross-correlation. The lensing data used in this analysis are described in Sec. III, and the analysis methods are detailed in Sec. IV. The results of the measurement, as well as null tests and systematic checks, are outlined in Sec. V, and we conclude in Sec. VI.

II. THEORETICAL BACKGROUND

The effects of cosmological gravitational lensing are encoded in the convergence field κ, which can be expressed as a weighted projection of the matter overdensity δ [33],

*nhand@berkeley.edu

$$\kappa(\hat{\mathbf{n}}) = \int_0^\infty dz W^\kappa(z)\delta(\chi(z)\hat{\mathbf{n}}, z). \quad (1)$$

Assuming a flat universe, the lensing kernel W^κ is

$$W^\kappa(z) = \frac{3}{2}\Omega_m H_\circ^2 \frac{(1+z)}{H(z)}\frac{\chi(z)}{c}\int_z^\infty dz_s p_s(z_s)\frac{\chi(z_s)-\chi(z)}{\chi(z_s)}, \quad (2)$$

where $p_s(z)$ is the normalized redshift distribution of source galaxies, $\chi(z)$ is the comoving distance to redshift z, $\hat{\mathbf{n}}$ is the direction on the sky, and $H_\circ$ and Ω_m are the present-day values of the Hubble and matter density parameters, respectively. We denote the kernel for the weak lensing of a source galaxy population with a redshift distribution $p_s(z) = dn/dz$ as $W^{\kappa_{\rm gal}}$.

For lensing of the CMB, the source redshift distribution can be approximated as $p_s(z) \simeq \delta_D(z - z_\star)$, where $z_\star \simeq 1090$ is the redshift of the surface of last scattering and δ_D is the Dirac delta function. This yields the following kernel [1]:

$$W^{\kappa_{\rm CMB}}(z) = \frac{3}{2}\Omega_m H_\circ^2 \frac{(1+z)}{H(z)}\frac{\chi(z)}{c}\left[\frac{\chi(z_\star)-\chi(z)}{\chi(z_\star)}\right]. \quad (3)$$

Using the Limber approximation [34,35], the cross power spectrum of the convergence fields due to CMB lensing and galaxy lensing can be computed to good precision as

$$C_\ell^{\kappa_{\rm CMB}\kappa_{\rm gal}} = \int_0^\infty \frac{dz}{c}\frac{H(z)}{\chi(z)^2} W^{\kappa_{\rm CMB}} W^{\kappa_{\rm gal}} P\left(k = \frac{\ell}{\chi}, z\right), \quad (4)$$

where $P(k, z)$ is the matter power spectrum evaluated at wave number k and redshift z. The degree of cross-correlation between the two convergence fields is determined by the overlap of the two kernels, weighted by the matter power spectrum. For comparison, the CMB lensing kernel $W^{\kappa_{\rm CMB}}$ and the galaxy lensing kernel $W^{\kappa_{\rm gal}}$ for the CS82 source population used in this work are shown in Fig. 1. The mean redshift of the product of $W^{\kappa_{\rm gal}}$ and $W^{\kappa_{\rm CMB}}$ is $z \sim 0.9$, illustrating that the cross power spectrum is sensitive to the amplitude of structure at intermediate redshifts.

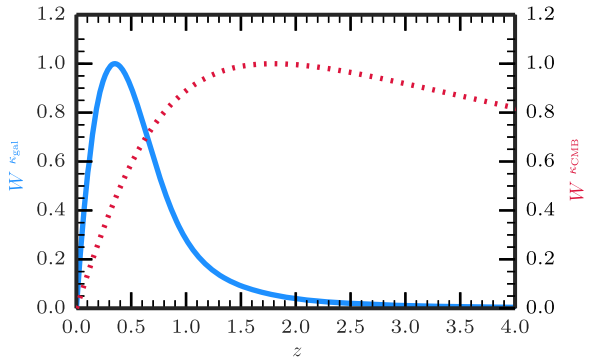

FIG. 1 (color online). The lensing kernel $W^{\kappa_{\rm gal}}$ (solid) for the CS82 redshift distribution of source galaxies [as given in Eq. (6)] and normalized to a unit maximum. For comparison, the kernel for CMB lensing [Eq. (3)] is shown as dashed, also normalized to a unit maximum.

III. CMB AND GALAXY LENSING DATA

A. ACT CMB lensing data

ACT is a 6-m telescope located in the Atacama desert in Chile [36–38]. The CMB temperature maps used in this work are made from observations taken during 2008–2010 in the 148 GHz frequency channel and have been calibrated to 2% accuracy as in [39]. The maps are centered on the celestial equator with a width of 3 deg in declination and 108 deg in right ascension and are identical to those used in [12].

The lensing convergence fields are reconstructed from the CMB temperature maps using the minimum variance quadratic estimator of [40] following the procedure used in [27]. The lensing deflection induces correlations in the Fourier modes of the previously uncorrelated, unlensed CMB. The lensing convergence is estimated from these Fourier correlations with a quadratic estimator:

$$\hat{\kappa}(\boldsymbol{L}) = N(\boldsymbol{L})\int \mathrm{d}^2\boldsymbol{l} f(\boldsymbol{L}, l)T(l)T(\boldsymbol{L}-\boldsymbol{l}), \quad (5)$$

where $\boldsymbol{l}$ and $\boldsymbol{L}$ are Fourier space coordinates, N is the normalization function, T is the temperature field, and f is a weighting function that maximizes the signal-to-noise ratio of the reconstructed convergence (see [40] for details). In the lensing reconstruction, we filter out temperature modes with a low signal-to-noise ratio, specifically those modes below $\ell = 500$ and above $\ell = 4000$. This filtering does not prevent the measurement of low-ℓ lensing modes, as the lensing signal at a given scale ℓ is obtained from temperature modes separated by ℓ [see Eq. (5)]. The maximum ℓ of included temperature modes is the only difference between the lensing maps used in this work and those in [12].

The final normalization is obtained in a two step process, as in [12]. A first-order approximation for the normalization is computed from the data power spectrum, with an additional, small correction factor (of order 10%) applied from Monte Carlo simulations, which are designed to match both the signal and noise properties of the ACT data. Finally, we obtain a simulated mean field map $\langle\hat{\kappa}\rangle$ from 480 Monte Carlo realizations of reconstructed CMB lensing convergence maps and subtract this mean field from the reconstructed ACT lensing maps. The simulated mean field is nonzero due to noise and finite-map effects giving rise to a small (∼5%) artificial lensing signal, which must be subtracted. Note that this set of 480 Monte Carlo

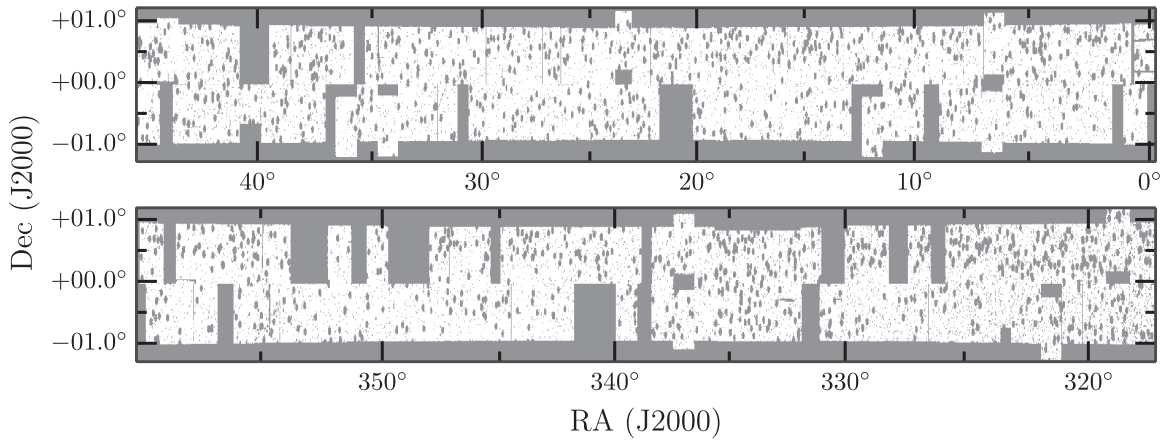

FIG. 2. The overlapping sky coverage of the ACT and CS82 data used in this work. Regions excluded as part of the CS82 mask are shown in grey, while unmasked regions, totaling 121 square degrees in area, are shown in white.

realizations is also used to estimate error bars on the final cross power spectrum measurement, as described in Sec. V.

B. CS82 Lensing Data

1. Data

The Canada-France-Hawaii Telescope Stripe 82 Survey is an i'-band survey of the so-called Stripe 82 region of sky along the celestial equator [41]. The survey was designed with the goal of covering a large fraction of Stripe 82 with high quality i'-band imaging suitable for weak lensing measurements. With this goal in mind, the CS82 survey was conducted under excellent seeing conditions: the point spread function (PSF) for CS82 varies between $0.4''$ and $0.8''$ over the entire survey with a median seeing of $0.6''$. In total, CS82 comprises 173 MegaCam i'-band images, with each image roughly one square degree in area with a pixel size of 0.187 arc seconds. The area covered by the survey is 160 deg^2 (129.2 deg^2 after masking out bright stars and other image artifacts), and the completeness magnitude is $i' \sim 24.1$ (AB magnitude, 5σ in a $2''$ aperture). Image processing is largely based on the procedures presented in [42,43]. Weak lensing shear catalogs were constructed using the state-of-the-art weak lensing pipeline developed by the CFHTLenS Collaboration which employs the *lens*fit shape measurement algorithm [44,45]. We refer to these publications for more in-depth details of the shear measurement pipeline.

Following [44] and [45], source galaxies are selected to have $w > 0$ and FITSCLASS $= 0$. Here, w represents an inverse variance weight accorded to each source galaxy by *lens*fit, and FITSCLASS is a flag to both remove stars and select galaxies with well-measured shapes (see details in [44]). After these cuts, the CS82 source galaxy density is 15.8 galaxies arc min^{-2}, and the effective weighted galaxy number density (see Eq. (1) in [45]) is 12.3 galaxies arc min^{-2}. Note that these numbers do not include any cuts on photometric redshift quality since for the purposes of this paper, we only need to know the CS82 source galaxy redshift distribution (see the following section). We derive the multiplicative shear calibration factor m in the same manner as [44], with the multiplicative shear measurement bias equal to $1 + m$.

Our reduction pipeline includes an automated masking routine to detect artifacts on an image-by-image basis and to mask out bright stars [43]. Each mask is manually inspected and modified when necessary (for example, to mask out faint satellite trails) to create a final set of masks. These high-resolution masks are then rebinned to a resolution of 1 arc min and combined into a larger single mosaic mask map for the full CS82 data. This mask is shown in Fig. 2, which shows the overlapping sky coverage of the ACT and CS82 data used in this work. The total area of the overlapping, unmasked region is 121 square degrees.

2. Source redshift distribution

As the CS82 i'-band imaging is deeper than the overlapping multicolor co-add data from SDSS [46], we cannot estimate a photometric redshift for each galaxy in our source catalog. However, for the purposes of this work, we do not require a photometric redshift estimate for each source galaxy. Instead, only the source redshift distribution is needed to predict the amplitude of the cross-correlation. We estimate this redshift distribution using the 30-band COSMOS photometric redshift catalog [47]. We select a random sample of COSMOS galaxies such that the i'-band magnitude distribution of the random sample matches the CS82 source catalog. We then fit the dn/dz from this matched sample, weighting each galaxy by w, the inverse variance weight accorded to each CS82 source galaxy. By using this weight, we account for the increase in the shape measurement noise at faint magnitudes (see Eq. (8) in [44]). Adopting the functional form from [48], the weighted source redshift distribution is given by

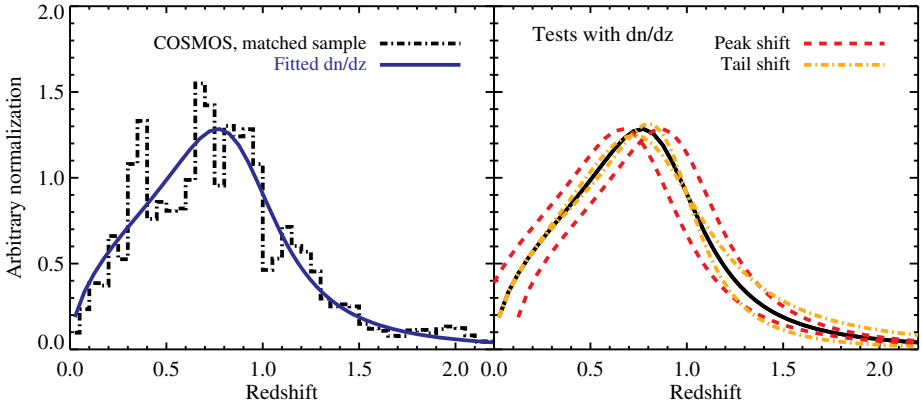

FIG. 3 (color online). Redshift distribution of CS82 source galaxies. Left: Redshift distribution for a matched sample of galaxies from the COSMOS survey. The blue solid line indicates our fit to the COSMOS matched sample. Right: We test how the amplitude of the theoretical lensing-lensing cross power spectrum changes when we vary the peak of the dn/dz (red, dashed lines) and the high-redshift tail of the distribution (orange, dash-dotted lines). These variations in the dn/dz lead to changes of order 10%–20% in the amplitude of the theoretical lensing-lensing cross power spectrum. Accurate estimates of dn/dz will be crucial for this kind of cross-correlation in the future.

$$\frac{dn}{dz} = A\frac{z^a + z^{ab}}{z^b + c}, \tag{6}$$

with $a = 0.531$, $b = 7.810$, $c = 0.517$, and $A = 0.688$. The source redshift distribution from the matched COSMOS sample is shown in Fig. 3.

There are uncertainties in our dn/dz estimate due to sample variance in the COSMOS data, errors in the COSMOS photometric redshifts, and the assumed parametric form for dn/dz. Estimating these uncertainties is a nontrivial task and is beyond the scope of this paper, as the main goal of this work is simply to present the detection of the cross-correlation. Nonetheless, to give some sense of the effects of uncertainty in dn/dz, we investigate how the predicted amplitude of the cross-correlation varies when we shift the peak and the high-redshift tail of dn/dz. For these tests, we shift the peak of dn/dz by $\Delta z = \pm 0.1$ and shift the high-redshift tail of dn/dz by varying the parameter b by $\pm 30\%$. These four test cases are shown in the right panel of Fig. 3. Again, we stress that these tests are not necessarily designed to represent the true underlying uncertainty in our dn/dz estimate (which is nontrivial to compute), but only to give some idea of how variations in dn/dz can affect the predicted amplitude of the cross-correlation.

When computing the theoretical cross power spectrum with fixed cosmological parameters using Eq. (4), we find that these dn/dz variations lead to changes of order 10%–20% in the amplitude of the theory curve. The largest amplitude change occurs when shifting the tail of the source distribution to higher redshift, with the other variations leading to comparable changes. As the CMB lensing kernel $W^{\kappa_{\rm CMB}}$ peaks at $z \sim 2$ with a broad tail to higher redshift, the degree of cross-correlation is quite sensitive to the tail of the source galaxy redshift distribution. Clearly, the interpretation of our results depends on the assumed dn/dz. In general, the high-redshift tail of the source redshift distribution is notoriously difficult to measure from photometric surveys. This is due in part to the Lyman-Balmer break degeneracy in photometric redshift codes for galaxies at $z \gtrsim 1.5$ (which requires difficult to obtain deep near-infrared or U-band imaging to be resolved), but also because high-redshift galaxies are faint and thus have more unreliable photometric redshifts. In conclusion, it is clear that future measurements of this kind will need to pay particular attention to systematics associated with the source redshift distribution.

3. CS82 shear maps

We create a series of maps for the CS82 data that follow a regular grid with a pixel size of 1 arc min and that are matched to the mosaic mask map described previously. To create shear maps, we closely follow the procedure outlined in [49] to account for the multiplicative shear measurement bias $(1 + m)$ and the weighting w. A normalized ellipticity map $M_{\rm e1}$ is constructed for the e_1 component of the ellipticity by summing e_1 over all source galaxies within in each pixel (x, y) and normalizing as

$$M_{\rm e1}(x, y) = \frac{\sum_i w_i e_{1,i}}{\sum_i w_i (1 + m_i)}, \tag{7}$$

where w_i is the inverse variance weight and m_i is the shear calibration factor associated with the $i^{\rm th}$ galaxy [44]. In a similar fashion, we also compute the following maps:

(i) $M_{\rm e2}(x, y)$: similar to $M_{\rm e1}(x, y)$ but for the e_2 component of the ellipticity.

(ii) $M_{\rm psf1}(x, y)$: similar to $M_{\rm e1}(x, y)$ but e_1 is replaced by an estimate of the e_1 component of the PSF ellipticity at galaxy position i.

(iii) $M_{\rm psf2}(x,y)$: similar to $M_{\rm e2}(x,y)$ but e_2 is replaced by an estimate of the e_2 component of the PSF ellipticity at galaxy position i.
(iv) $M_{\rm bmode1}(x,y)$: the first B-mode component of the ellipticity, which is equal to $-M_{\rm e2}(x,y)$.
(v) $M_{\rm bmode2}(x,y)$: the second B-mode component of the ellipticity, which is equal to $M_{\rm e1}(x,y)$.

We also create a set of 500 random maps for each component of the ellipticity. In these maps, the position of each galaxy is preserved, but for each realization, we rotate source galaxies by a random position angle. This process ensures that the maps have the same shape noise as the CS82 ellipticity maps but do not contain a cosmological shear signal. We use these random maps for null tests in cross-correlation with the true ACT data (see Sec. V).

Finally, as discussed in [45], 25% of the CFHT Legacy Survey fields have a significant PSF residual and are rejected for cosmic shear studies [16,17]. However, this cross-correlation analysis should be much less sensitive to PSF-related errors in comparison to cosmic shear measurements because CS82 PSF patterns should be uncorrelated with the ACT CMB lensing signal. In addition, [49] found that it was not necessary to reject these fields. Nonetheless, it is possible that the PSF pattern correlates with the ACT signal simply by chance. The $M_{\rm psf}(x,y)$ maps are designed to test and rule out this possibility (see the discussion of null tests in Sec. V).

IV. METHODS

A. Power spectrum estimation

The cross-correlation of the ACT CMB lensing and CS82 galaxy lensing convergence fields is computed in Fourier space. The choice to reconstruct the correlation in Fourier space rather than real space was made in order to limit correlations between different data bins, which can complicate the interpretation of the final measurement. Furthermore, this method minimizes the total number of Fourier transforms needed, which reduces noise due to windowing and edge effects. In order to obtain an unbiased estimate of the cross spectrum, we follow a procedure similar to the steps outlined in previous ACT power spectrum analyses [12,50], which properly account for the coupling of Fourier modes induced by filtering and windowing effects. The notation and terminology in this section closely follows that of these previous ACT analyses.

1. The data window

First, the real space ACT convergence map is repixelized to match the resolution (1 arc min) of the CS82 data. Then, the ACT data and CS82 ellipticity maps are spatially divided into two noncontiguous patches on which the cross spectrum estimation is computed separately. The two patches are divided at zero right ascension due to a coincidental discontinuity in the CS82 imaging at this location. This divides the original map into two roughly equal area patches. We denote the separate patches with greek indices, such that patch α of the two CS82 ellipticity maps at position $\boldsymbol{\theta} = (x,y)$ is denoted as $M^{\alpha}_{e1}(x,y)$ and $M^{\alpha}_{e2}(x,y)$. Similarly, patch α of the repixelized ACT convergence map is denoted as $M^{\alpha}_{\kappa_{\rm CMB}}(x,y)$.

Both the CS82 and ACT data patches are multiplied in real space by a tapering function and the CS82 mask map, which masks out image artifacts and bright point sources. The tapering function minimizes noise introduced by the patch edges in Fourier space. It is generated by convolving a map that is unity in the center and zero over 10 pixels at the edges with a Gaussian of full width at half maximum of $5'$. The window function in real space is the product of these two components—the tapering function and the CS82 mask. In the following discussion, the window function is denoted by K^{α} and the windowed data patches are denoted as $\tilde{M}^{\alpha}_{i}$, where $i \in [e1, e2, \kappa_{\rm CMB}]$.

2. Galaxy lensing convergence reconstruction

We reconstruct the CS82 convergence field in Fourier space from the windowed ellipticity patches, following the prescription outlined in [51]. The galaxy lensing convergence field in Fourier space $\tilde{M}^{\alpha}_{\kappa_{\rm gal}}(\ell)$ is given by

$$\tilde{M}^{\alpha}_{\kappa_{\rm gal}}(\ell) = F_{\ell}\left[\tilde{M}^{\alpha}_{e1}(\ell)\frac{\ell_x^2-\ell_y^2}{\ell^2} + \tilde{M}^{\alpha}_{e2}(\ell)\frac{2\ell_x\ell_y}{\ell^2}\right], \quad (8)$$

where the wave vector $\boldsymbol{\ell} = (\ell_x, \ell_y) = 2\pi/\boldsymbol{\theta}$ is defined as the two-dimensional Fourier analog of $\boldsymbol{\theta}$, $\ell^2 = \ell_x^2 + \ell_y^2$, and F_{ℓ} is a Gaussian smoothing filter of full width at half maximum of $2'$.

3. Mode coupling

A 2D pseudospectrum is computed from the windowed convergence fields as

$$\tilde{C}^{\kappa_{\rm CMB}\kappa_{\rm gal}}_{\ell} = {\rm Re}[\tilde{M}^{\star}_{\kappa_{\rm CMB}}(\ell)\tilde{M}_{\kappa_{\rm gal}}(\ell)], \quad (9)$$

where the patch index has been suppressed for clarity. The 1D binned spectrum $\tilde{C}_b$ is computed by averaging the 2D spectrum in annular bins

$$\tilde{C}^{\kappa_{\rm CMB}\kappa_{\rm gal}}_{b} = \sum_{\ell} P_{b\ell}\tilde{C}^{\kappa_{\rm CMB}\kappa_{\rm gal}}_{\ell}, \quad (10)$$

where $P_{b\ell}$ is the binning matrix, which is defined to be zero when ℓ is outside the annulus defined by bin index b and unity otherwise.

Noting that the windowing operation in real space corresponds to a convolution in Fourier space and using Eqs. (8) to (10), we can express the binned 1D pseudospectrum $\tilde{C}_b$ in terms of the underlying spectrum C_{ℓ} as

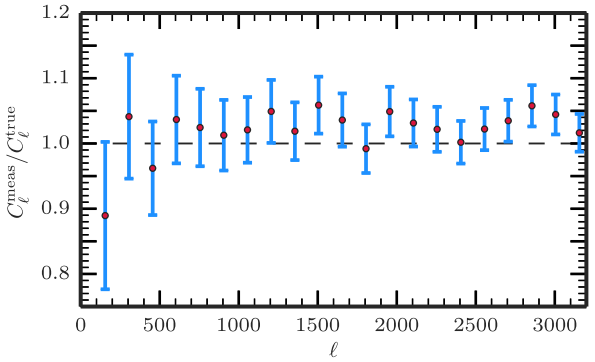

FIG. 4 (color online). The ratio of the auto power spectrum of simulated lensing convergence maps measured using our analysis pipeline $C_\ell^{\rm meas}$ to the true, input auto spectrum $C_\ell^{\rm true}$. The analysis pipeline described in Sec. IV properly recovers the input spectrum from simulations.

$$\tilde{C}_b^{\kappa_{\rm CMB}\kappa_{\rm gal}} = \sum_{\ell,\ell'} P_{b\ell} |K(\ell - \ell')|^2 F_{\ell'} C_{\ell'}^{\kappa_{\rm CMB}\kappa_{\rm gal}}, \quad (11)$$

where K is the three-component window function discussed previously. We relate this quantity to a binned version of the true spectrum C_b via an inverse binning operator $Q_{\ell b}$, which is unity when $\ell \in b$ and zero otherwise,

$$\begin{aligned}\tilde{C}_b^{\kappa_{\rm CMB}\kappa_{\rm gal}} &= \sum_{\ell,\ell',b'} P_{b\ell} |K(\ell - \ell')|^2 F_{\ell'} Q_{\ell' b'} C_{b'}^{\kappa_{\rm CMB}\kappa_{\rm gal}}, \\ &\equiv \sum_{b'} M_{bb'} C_{b'}^{\kappa_{\rm CMB}\kappa_{\rm gal}}, \end{aligned} \quad (12)$$

where $M_{bb'}$ is the mode-coupling matrix, which is well behaved and stable to inversion. Finally, we define the unbiased estimator of the power spectrum (denoted by a circumflex) as

$$\hat{C}_b^{\kappa_{\rm CMB}\kappa_{\rm gal}} = \sum_{b'} M_{bb'}^{-1} \tilde{C}_{b'}^{\kappa_{\rm CMB}\kappa_{\rm gal}}. \quad (13)$$

We use Eq. (13) to estimate the cross power spectrum for each patch and compute the final cross power spectrum as the mean of the spectra from the two individual patches.

B. Pipeline validation

We use simulated galaxy lensing maps to validate the power spectrum analysis steps described in the previous section. The simulated maps are constructed using the shear signal from the N-body simulations described in [52]. Projected shear and convergence "tiles" are produced for 25 separate lines of sight in the simulation. Each tile covers an area of 12.8 deg^2 and has a pixel size of 0.21′. For simplicity, we use shear and convergence maps constructed using source galaxies at a single redshift of $z = 0.73$. As the purpose of the simulation maps is only to verify the analysis pipeline, a more realistic dn/dz is not required.

We repixelize the 25 simulated tiles to match the pixel size of the CS82 data (1 arc min) and use these tiles to construct a map with equal size and area to the map used in the data analysis. We then multiply the shear maps by the CS82 mask map, reconstruct the convergence in Fourier space using Eq. (8), and estimate the convergence auto power spectrum using the analysis steps outlined in the previous section. Figure 4 shows the result of this calculation, plotting the ratio of the reconstructed auto spectrum to the true, input spectrum. The analysis pipeline accurately recovers the input power spectrum, within the measured errors.

V. RESULTS

A. The CMB lensing: Galaxy lensing cross power spectrum

The cross power spectrum of the ACT CMB lensing and CS82 galaxy lensing convergence maps is shown in Fig. 5. The error bars on the data points are computed by cross-correlating 480 Monte Carlo realizations of simulated reconstructed CMB lensing maps with the true CS82 data. The simulated CMB lensing maps are constructed to match both the signal and noise properties of the ACT data maps. As a consistency check, we note that these error bars agree well with the theoretical expectation, which is computed using the auto spectra of the individual maps. Specifically, the analytic error bars are proportional to $\sqrt{C_\ell^{\kappa_{\rm CMB}\kappa_{\rm CMB}} C_\ell^{\kappa_{\rm gal}\kappa_{\rm gal}}}$ and an additional factor that accounts for the number of independent pixels in each data bin. We assume in both methods that the maps are uncorrelated, which is a valid approximation since both maps are noisy such that $C_\ell^{\kappa_{\rm CMB}\kappa_{\rm CMB}} C_\ell^{\kappa_{\rm gal}\kappa_{\rm gal}} \gg (C_\ell^{\kappa_{\rm CMB}\kappa_{\rm gal}})^2$.

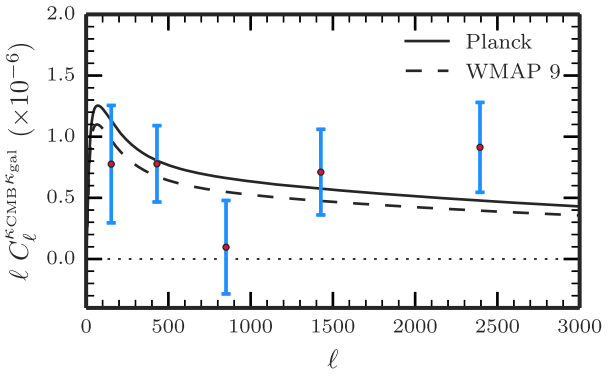

FIG. 5 (color online). The CMB lensing-galaxy lensing convergence cross power spectrum (red points), measured using ACT and CS82 data. Error bars are computed using Monte Carlo methods (see text), and the significance of the measurement is 4.2σ. The solid and dashed black lines show the expected power spectra assuming the Planck + lensing + WP + highL and WMAP9 + eCMB cosmological models, respectively. The theoretical spectra shown correspond to $A = 1$, and relative to these models, the best-fit amplitudes to our data are $A^{\rm Planck} = 0.78 \pm 0.18$ and $A^{\rm WMAP} = 0.92 \pm 0.22$.

Using Monte Carlo methods to estimate the error bars allows us to calculate the full covariance matrix. Neighboring bins are approximately ∼10% anticorrelated, while nearly all other off-diagonal correlations are less than 5% of the bin autocorrelation. We account for the full covariance matrix when computing measurement significances.

The theoretical expectation for the cross power spectrum obtained by evaluating Eq. (4) is also shown in Fig. 5. We consider two separate cosmological models for comparison. First, we use the best-fit Planck + lensing + WP + highL parameter set with $\sigma_8 = 0.827$ [53], where WP refers to the inclusion of WMAP polarization data and highL refers to the inclusion of ACT and South Pole Telescope high-ℓ CMB data in the parameter likelihood. Second, we consider the WMAP9 + extended CMB (eCMB) model with $\sigma_8 = 0.81$ [54], where eCMB refers to the usage of high-ℓ ACT and South Pole Telescope CMB data in the parameter likelihood. In both calculations, the nonlinear matter power spectrum (HALOFIT, [55,56]) is used.

We define a parameter A for the amplitude of the cross spectrum relative to the two models considered here, defined such that $A = 1$ corresponds to the fiducial model. We compute the amplitude likelihood for both the Planck and WMAP models, assuming no uncertainties in the CS82 source distribution. Relative to the Planck fiducial model, we obtain a best-fit amplitude $A^{\rm Planck} = 0.78 \pm 0.18$, with $\chi^2 = 3.58$ and $\chi^2/\nu = 0.90$ for $\nu = 4$ degrees of freedom. Relative to the WMAP9 model, we measure an amplitude $A^{\rm WMAP} = 0.92 \pm 0.22$, with $\chi^2 = 3.68$ and $\chi^2/\nu = 0.92$. The significance is computed as the square root of the difference between the chi-squared values of the null line ($A = 0$) and the best-fit theoretical spectrum: $(\Delta\chi^2)^{1/2} = \sqrt{\chi^2_{\rm null} - \chi^2_{\rm theory}}$. With a measured value of $\chi^2_{\rm null} = 21.67$, the best-fit theoretical model is favored over the null hypothesis with a significance of 4.2σ (for both the Planck and WMAP9 models).

Since the amplitude of the cross spectrum scales as the square of the amplitude of density fluctuations, this measurement corresponds to a ∼12% constraint on the amplitude of structure at intermediate redshifts, $z \sim 0.9$, which corresponds to the mean redshift of the product of the CMB lensing and galaxy lensing kernels (see Fig. 1). This constraint on σ_8 is given as an approximate benchmark for comparison to other current growth of structure measurements, rather than a robust cosmological constraint. We choose not to perform a more detailed cosmological interpretation of this measurement for several reasons. As discussed in Sec. III, uncertainties in the source galaxy redshift distribution must be well understood before achieving accurate constraints, as dn/dz errors propagate to uncertainties in the predicted amplitude of the theoretical cross power spectrum. Furthermore, as noted recently in [57,58], the CMB lensing-galaxy lensing power spectrum is contaminated, at some level, by a cross-correlation term between CMB lensing and galaxy intrinsic alignment. The magnitude of this contamination must be carefully calibrated before using the CMB lensing-galaxy lensing cross-correlation for precision cosmology in the future.

B. Null tests

We verify our pipeline and measured cross power spectrum with a series of null tests. The first test uses 500 realizations of randomized galaxy lensing shear maps, described previously in Sec. III. We compute the mean cross power spectrum between the true ACT convergence field and these random maps. Shown in the top panel of Fig. 6, this mean correlation is consistent with zero, with $\chi^2 = 3.4$ for 5 degrees of freedom; the probability of random deviates with the same covariances to exceed this chi-squared is 63%. Note that the set of 500 randomized shear maps do not contain a cosmological shear signal and thus, can only be used as a null test rather than to estimate error bars for the final cross spectrum measurement. We also create a set of 58 "shuffled" ACT maps by shifting the true ACT data in intervals of 0.75° along the right ascension

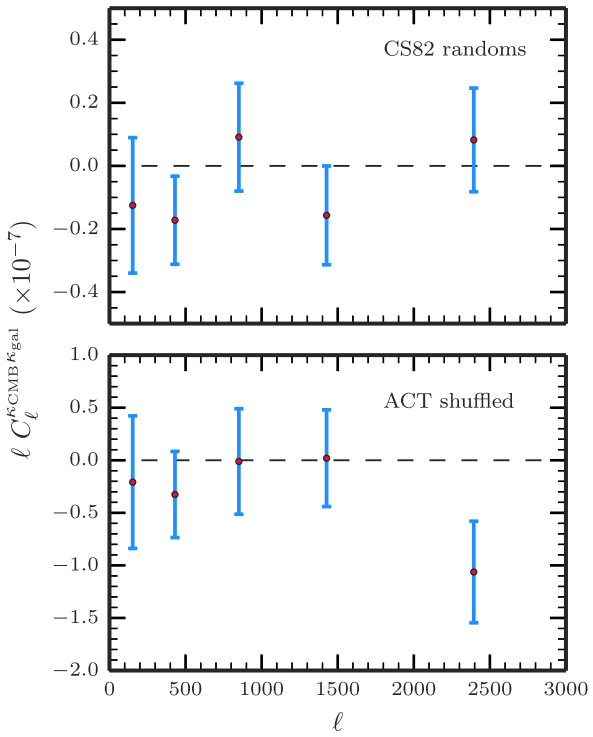

FIG. 6 (color online). Two successful null tests, both consistent with zero. Top: The mean correlation between 500 randomized galaxy lensing maps and the true ACT data. Bottom: The mean correlation between the true CS82 data and 58 ACT "shuffled" maps, constructed by shifting the data in intervals of 0.75° along the right ascension direction. The probabilities to exceed the measured χ^2 for these tests are 63% and 34%, respectively. Note that the scaling of the y-axis here is an order of magnitude smaller than the y-axis of Fig. 5.

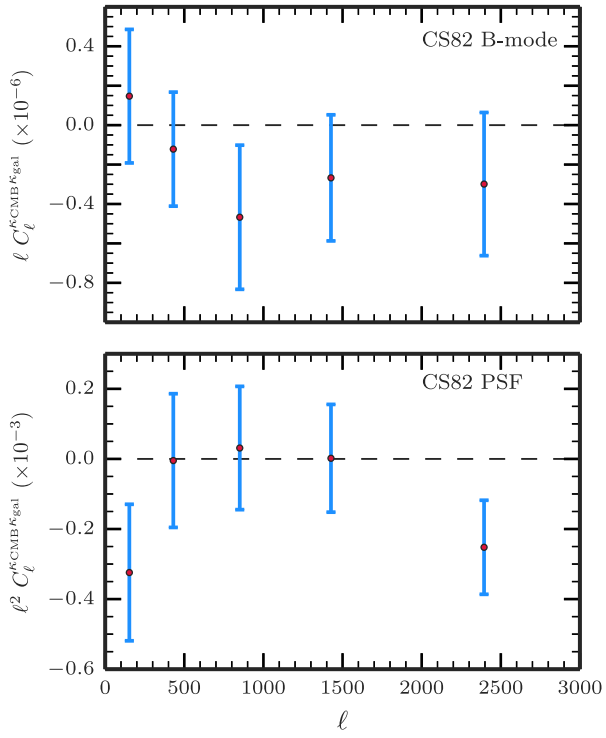

FIG. 7 (color online). Two tests of the CS82 galaxy lensing data, both consistent with zero. The data points show the correlations between the ACT data and the CS82 B-mode ellipticity data (top) and the PSF ellipticity data (bottom). The probabilities to exceed the measured χ^2 for these tests are 55% and 13%, respectively. Note that the quantity $\ell^2 C_\ell$ is plotted in the bottom panel in order to increase the dynamic range of the plot.

direction. The mean of the cross-correlation between these shuffled maps and the CS82 convergence data is shown in the lower panel of Fig. 6. This mean correlation is also consistent with null signal, with $\chi^2 = 5.7$ and a probability to exceed of 34%. The error bars for each of these measurements are computed using the full covariance matrix as determined from the Monte Carlo realizations, as was done for the true data.

We also perform two specific tests of the CS82 shear data, designed to check for any unexpected correlations due to possible systematic issues with the galaxy lensing data. We compute the cross power spectrum using the same methods outlined in Sec. IV, but replace the CS82 ellipticity data with (1) the B-mode ellipticity maps $M_{\rm bmode1/2}$ and (2) the PSF ellipticity maps $M_{\rm psf1/2}$. The B-mode ellipticity is obtained using the transformation (e_1, e_2) to $(-e_2, e_1)$, and in the absence of systematics, should vanish. The cross power spectrum between the ACT data and the B-mode convergence data is shown in the top panel of Fig. 7. As expected, the measurement is consistent with null signal, with $\chi^2 = 4.0$ for 5 degrees of freedom, corresponding to a 55% probability that the chi-squared of random noise would exceed the measured value. The bottom panel of Fig. 7 shows the correlation between the ACT data and the PSF data. The result is also consistent with zero, with $\chi^2 = 8.6$ and a probability to exceed of 13%. The error bars for both spectra are computed from Monte Carlo estimates, as done previously.

VI. CONCLUSIONS

We have cross-correlated CMB lensing and galaxy lensing convergence maps and measured the lensing-lensing cross power spectrum for the first time—at 4.2σ significance. This cross power is a direct gravitational measurement of the distribution of mass at redshifts ∼0.9. The measurement constrains the amplitude of structure to an uncertainty of ∼12%, although contamination from galaxy intrinsic alignments and errors in the dn/dz must be carefully considered for more precise cosmological constraints. Our method is remarkably robust to instrumental and astrophysical systematic errors. It is performed with a cross-correlation of mass measurements relying on completely different measurement techniques and photon wavelengths, which few systematics can survive. Despite the moderate detection significance, this robustness makes a first measurement of this cross-correlation signal a valuable confirmation of the ΛCDM model for large-scale structure at intermediate redshifts.

In just the next few years, measurements of lensing-lensing cross-correlations are expected to increase in signal-to-noise by more than an order of magnitude [28–32]. CMB lensing-galaxy lensing cross-correlations have the potential to greatly contribute to cosmology in two main ways. First, they can serve as a calibrator of instrumental systematics, which may potentially limit future optical and infrared weak lensing surveys. By adding information from lensing-lensing cross-correlations to weak lensing power spectra, additive and multiplicative biases can be precisely constrained, which will allow future weak lensing surveys to reach their full cosmological potential (see e.g., [22,23]). Second, they will serve as an independent, robust measurement of the amplitude of structure at intermediate redshifts. When combined with probes at higher redshift (e.g., CMB lensing) and lower redshift (e.g., weak lensing), lensing-lensing cross-correlations will help measure the growth of structure across a wide range of redshifts. This, in turn, will allow for powerful constraints on the sum of neutrino masses and the properties of dark energy. This work thus demonstrates an important proof of concept of an exciting new cosmological probe.

ACKNOWLEDGMENTS

We thank the CFHTLenS team for their pipeline development and verification upon which much of this survey pipeline was built. We also thank Jeff Newman and Peter Freeman for helpful conversations about statistical analysis. This work was supported by the U.S. National Science

Foundation through Grants No. AST-0408698 and No. AST-0965625 for the ACT project, as well as Grants No. PHY-0855887 and No. PHY-1214379. Funding was also provided by Princeton University, the University of Pennsylvania, and a Canada Foundation for Innovation (CFI) award to UBC. ACT operates in the Parque Astronómico Atacama in northern Chile under the auspices of the Comisión Nacional de Investigación Científica y Tecnológica de Chile (CONICYT). Computations were performed on the GPC supercomputer at the SciNet HPC Consortium. SciNet is funded by the CFI under the auspices of Compute Canada, the Government of Ontario, the Ontario Research Fund: Research Excellence, and the University of Toronto. This work was based on observations obtained with MegaPrime/MegaCam, a joint project of CFHT and CEA/DAPNIA, at the Canada-France-Hawaii Telescope (CFHT), which is operated by the National Research Council (NRC) of Canada, the Institut National des Science de l'Univers of the Centre National de la Recherche Scientifique (CNRS) of France, and the University of Hawaii. The Brazilian partnership on CFHT is managed by the Laboratório Nacional de Astrofísica (LNA). This work made use of the CHE cluster, managed and funded by ICRA/CBPF/MCTI, with financial support from FINEP and FAPERJ. We thank the support of the Laboratório Interinstitucional de e-Astronomia (LIneA). N. H. is supported by the National Science Foundation Graduate Research Fellowship under Grant No. DGE-1106400 and the Berkeley Fellowship for Graduate Study. T. E. is supported by the Deutsche Forschungsgemeinschaft through Project No. ER 327/3-1 and by the Transregional Collaborative Research Centre TR 33 "The Dark Universe." B. M. acknowledges financial support from the CAPES Foundation Grant No. 12174-13-0. C. H. acknowledges support from the European Research Council under the EC FP7 Grant No. 240185. H. Y. S. acknowledges the support from Marie-Curie International Incoming Fellowship (FP7-PEOPLE-2012-IIF/327561), Swiss National Science Foundation (SNSF) and NSFC of China under Grant No. 11103011. This work was supported by World Premier International Research Center Initiative (WPI Initiative), MEXT, Japan. H. H. is supported by the Marie Curie IOF 252760, by a CITA National Fellowship, and the DFG Grant No. Hi 1495/2-1. J. P. K. acknowledges support from the ERC advanced grant LIDA and from CNRS. We acknowledge support from NSF Grant No. 1066293 and thank the Aspen Center for Physics for hospitality during the writing of this paper.

[1] A. Lewis and A. Challinor, Phys. Rep. **429**, 1 (2006).
[2] D. Munshi, P. Valageas, L. van Waerbeke, and A. Heavens, Phys. Rep. **462**, 67 (2008).
[3] C. Feng, G. Aslanyan, A. V. Manohar, B. Keating, H. P. Paar, and O. Zahn, Phys. Rev. D **86**, 063519 (2012).
[4] L. E. Bleem *et al.* (SPT Collaboration), Astrophys. J. **753**, L9 (2012).
[5] G. P. Holder *et al.* (SPT Collaboration), Astrophys. J. **771**, L16 (2013).
[6] P. A. R. Ade, N. Aghanim, C. Armitage-Caplan, M. Arnaud, M. Ashdown, F. Atrio-Barandela, J. Aumont, C. Baccigalupi, A. J. Banday *et al.* (Planck Collaboration), Astron. Astrophys. **571**, A18 (2014).
[7] B. D. Sherwin *et al.* (ACT Collaboration), Phys. Rev. D **86**, 083006 (2012).
[8] J. E. Geach *et al.* (SPT Collaboration), Astrophys. J. **776**, L41 (2013).
[9] W. Hu, Astrophys. J. **522**, L21 (1999).
[10] R. de Putter, O. Zahn, and E. V. Linder, Phys. Rev. D **79**, 065033 (2009).
[11] S. Das, R. de Putter, E. V. Linder, and R. Nakajima, J. Cosmol. Astropart. Phys. 11 (2012) 011.
[12] S. Das *et al.*, J. Cosmol. Astropart. Phys. 04 (2014) 014.
[13] B. D. Sherwin *et al.* (ACT Collaboration), Phys. Rev. Lett. **107**, 021302 (2011).
[14] A. van Engelen *et al.* (SPT Collaboration), Astrophys. J. **756**, 142 (2012).
[15] P. A. R. Ade, N. Aghanim, C. Armitage-Caplan, M. Arnaud, M. Ashdown, F. Atrio-Barandela, J. Aumont, C. Baccigalupi, A. J. Banday *et al.* (Planck Collaboration), Astron. Astrophys. **571**, A17 (2014).
[16] J. Benjamin *et al.* (CFHTLenS Collaboration), Mon. Not. R. Astron. Soc. **431**, 1547 (2013).
[17] C. Heymans *et al.* (CFHTLenS Collaboration), Mon. Not. R. Astron. Soc. **432**, 2433 (2013).
[18] M. Kilbinger *et al.* (CFHTLenS Collaboration), Mon. Not. R. Astron. Soc. **430**, 2200 (2013).
[19] W. Hu, Phys. Rev. D **65**, 023003 (2001).
[20] L. Hollenstein, D. Sapone, R. Crittenden, and B. M. Schäfer, J. Cosmol. Astropart. Phys. 04 (2009) 012.
[21] T. Namikawa, S. Saito, and A. Taruya, J. Cosmol. Astropart. Phys. 12 (2010) 027.
[22] A. Vallinotto, Astrophys. J. **759**, 32 (2012).
[23] S. Das, J. Errard, and D. Spergel, arXiv:1311.2338.
[24] A. Vallinotto, Astrophys. J. **778**, 108 (2013).
[25] C. M. Hirata, S. Ho, N. Padmanabhan, U. Seljak, and N. A. Bahcall, Phys. Rev. D **78**, 043520 (2008).
[26] K. M. Smith, O. Zahn, and O. Doré, Phys. Rev. D **76**, 043510 (2007).
[27] S. Das *et al.* (ACT Collaboration), Phys. Rev. Lett. **107**, 021301 (2011).

[28] M. D. Niemack *et al.* (ACTPol Collaboration), Proc. SPIE Int. Soc. Opt. Eng. **7741**, 77411S (2010).
[29] J. E. Austermann *et al.* (SPTPol Collaboration), Proc. SPIE Int. Soc. Opt. Eng. **8452**, 84521E (2012).
[30] K. Arnold *et al.* (POLARBEAR Collaboration), Proc. SPIE Int. Soc. Opt. Eng. **7741**, 77411E (2010).
[31] http://www.darkenergysurvey.org/.
[32] http://www.naoj.org/Projects/HSC/index.html.
[33] M. Bartelmann and P. Schneider, Phys. Rep. **340**, 291 (2001).
[34] D. N. Limber, Astrophys. J. **119**, 655 (1954).
[35] N. Kaiser, Astrophys. J. **388**, 272 (1992).
[36] J. W. Fowler *et al.* (ACT Collaboration), Appl. Opt. **46**, 3444 (2007).
[37] D. S. Swetz *et al.* (ACT Collaboration), Astrophys. J. Suppl. Ser. **194**, 41 (2011).
[38] R. Dünner *et al.* (ACT Collaboration), Astrophys. J. **762**, 10 (2013).
[39] A. Hajian *et al.* (ACT Collaboration), Astrophys. J. **740**, 86 (2011).
[40] W. Hu and T. Okamoto, Astrophys. J. **574**, 566 (2002).
[41] T. Erben *et al.* (to be published).
[42] T. Erben *et al.* (CARS Collaboration), Astron. Astrophys. **493**, 1197 (2009).
[43] T. Erben *et al.* (CFHTLenS Collaboration), Mon. Not. R. Astron. Soc. **433**, 2545 (2013).
[44] L. Miller *et al.* (CFHTLenS Collaboration), Mon. Not. R. Astron. Soc. **429**, 2858 (2013).
[45] C. Heymans *et al.* (CFHTLenS Collaboration), Mon. Not. R. Astron. Soc. **427**, 146 (2012).
[46] J. Annis *et al.*, Astrophys. J. **794**, 120 (2014).
[47] O. Ilbert *et al.* (COSMOS Collaboration), Astrophys. J. **690**, 1236 (2009).
[48] L. Fu *et al.* (CFHTLS Collaboration), Astron. Astrophys. **479**, 9 (2008).
[49] L. Van Waerbeke *et al.* (CFHTLenS Collaboration), Mon. Not. R. Astron. Soc. **433**, 3373 (2013).
[50] S. Das *et al.* (ACT Collaboration), Astrophys. J. **729**, 62 (2011).
[51] N. Kaiser and G. Squires, Astrophys. J. **404**, 441 (1993).
[52] J. Harnois-Déraps, S. Vafaei, and L. Van Waerbeke, Mon. Not. R. Astron. Soc. **426**, 1262 (2012).
[53] P. A. R. Ade, N. Aghanim, C. Armitage-Caplan, M. Arnaud, M. Ashdown, F. Atrio-Barandela, J. Aumont, C. Baccigalupi, A. J. Banday *et al.* (Planck Collaboration), Astron. Astrophys. **571**, A16 (2014).
[54] G. Hinshaw *et al.* (WMAP Collaboration), Astrophys. J. Suppl. Ser. **208**, 19 (2013).
[55] R. E. Smith, J. A. Peacock, A. Jenkins, S. D. M. White, C. S. Frenk, F. R. Pearce, P. A. Thomas, G. Efstathiou, and H. M. P. Couchman, Mon. Not. R. Astron. Ser. **341**, 1311 (2003).
[56] R. Takahashi, M. Sato, T. Nishimichi, A. Taruya, and M. Oguri, Astrophys. J. **761**, 152 (2012).
[57] A. Hall and A. Taylor, Mon. Non. R. Astron. Ser. **443**, L119 (2014).
[58] M. A. Troxel and M. Ishak, Phys. Rev. D **89**, 063528 (2014).